Optical properties of $CsCu_2X_3$ (X=Cl, Br and I): A comparative study between hybrid time-dependent density-functional theory and the Bethe-Salpeter equation

Jiuyu Sun and Carsten A. Ullrich
Department of Physics and Astronomy, University of Missouri, Columbia, Missouri 65211, USA
(Dated: July 13, 2021)

The cesium copper halides $CsCu_2X_3$ (X=Cl, Br and I) are a class of all-inorganic perovskites with interesting and potentially useful optical properties, characterized by distinct excitonic features. We present a computational study of the optical absorption spectra of $CsCu_2X_3$, comparing time-dependent density-functional theory (TDDFT) and the Bethe-Salpeter equation (BSE), using *GW* quasiparticle band structures as input. The TDDFT calculations are carried out using several types of global hybrid exchange-correlation functionals. It is found that an admixture of nonlocal exchange determined by the dielectric constant produces optical spectra in excellent agreement with the BSE. Thus, hybrid TDDFT emerges as a promising first-principles approach for excitonic effects in solids.

I. INTRODUCTION

Low-dimensional (quasi-2D, 1D, and 0D) hybrid organic-inorganic lead halides have been intensely investigated as promising luminescent materials [1–6]. The low dimensionality of these structures gives rise to quantum confinement effects, which yield more stable excitons at room temperature, and therefore enhanced luminescence properties [7–9]. However, the practical applications of these materials are limited by the instability and toxicity caused by the organic constituents and the presence of Pb ions [10, 11].

Recently, all-inorganic low-dimensional Cu halides have attracted increasing attention, such as quasi-0D $Cs_3Cu_2X_5$ [12–15], quasi-1D Rb_2CuX_3 [16, 17], and quasi-1D $CsCu_2X_3$ (X= Cl, Br, I) [18–20]. It has been reported that these classes of halides exhibit high photoluminescence quantum efficiencies (PLQEs), as well as wide, tunable ranges of emission wavelengths. These highly desirable properties can be attributed to the presence of self-trapped excitons [21–23]: thanks to the reduced dimensionality and the relatively soft crystal lattices, the excitons in these materials are strongly self-trapped, which results in a large Stokes shift and a broad spectrum of photoemission [24, 25]. Clearly, a theoretical understanding of the excitons in these materials is important for improving the PLQE. A complete description including the coupling of electronic and lattice degrees of freedom would be a highly challenging task; however, even without lattice relaxation effects, an accurate first-principles study of excitons in Cu halides will be a crucial step towards a more complete picture of the optical properties in these materials.

Due to the weakened Coulomb screening, excitons in low-dimensional Cu halides are much more strongly bound than in bulk [17–19]. The excitonic binding energy is reported to be several hundreds of meV [17, 18], which is one to two orders of magnitude larger than those in the popular 3D lead halide based perovskites ($CsPbX_3$ [26–28] and $CH_3NH_3PbX_3$ [29, 30]). Excitons are collective excitations within a many-body system, and thus cannot be properly described within a single-quasiparticle (QP) picture. To study the excitons, the standard method is via many-body perturbation theory, using the *GW* approximation for the QP states [31] and the Bethe-Salpeter equation (BSE) for the optical spectra [32–34]. However, this approach becomes extremely expensive for large supercells, which makes it unaffordable for defective or lattice-distorted systems.

An alternative approach is density functional theory (DFT) and its dynamical counterpart, time-dependent density functional theory (TDDFT) [35–38]. A very widely used generalization of (TD)DFT [39–42] is based on hybrid functionals, where a fraction of nonlocal Fock exchange is combined with (semi)local exchange and correlation [43–46]. The prefactor of the Fock exchange part can be determined either by empirical fitting [47–49], or by using a nonempirical value dependent on the dielectric function [50–52]. In ground-state DFT, hybrid xc functionals have gained increased popularity for calculating electronic band structures, since they offer a practical solution to DFT's band-gap problem [53–64]. Although hybrid functionals have been applied for ground-state band structures in perovskites [65–69], there have so far been only few applications of hybrid functionals for the optical spectra of perovskites [70].

In this paper, we explore the performance of hybrid functionals for calculating the optical properties, in particular the excitons, of $CsCu_2X_3$ (X= Cl, Br, I) (see Fig. 1). As mentioned, this class of low-dimensional perovskites has excitonic binding energies over 100 meV, which presents an ideal test case to examine the performance of hybrid TDDFT for excitonic effects. Detailed experimental results for the optical absorption spectra and exciton binding energies of $CsCu_2X_3$ are not available at present; therefore, we base our assessment of hybrid TDDFT on a comparison with reference results from state-of-the-art *GW*-BSE; to our knowledge, QP band structures and optical properties from *GW*-BSE have not been previously reported for these materials.

We apply both empirical and nonempirical hybrid functionals, in which the admixture of nonlocal exchange is fixed or material-dependent, respectively. Comparison between different hybrid functionals and the BSE

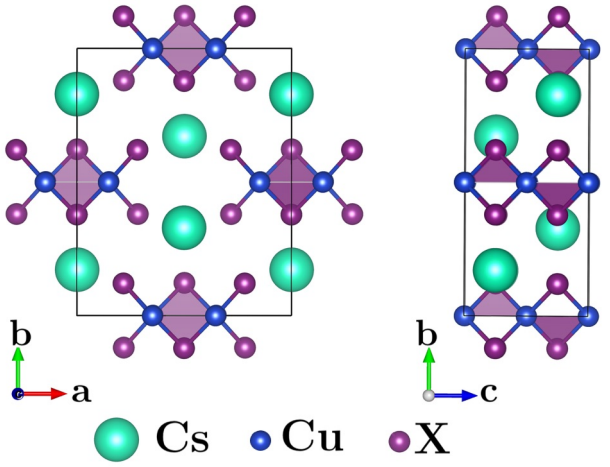

FIG. 1. Crystalline geometry of $CsCu_2X_3$ (X= Cl, Br, I). The lattice features 1D chains of $[Cu_2X_3]^-$ units along the c axis, separated by rows of Cs^+ ions [18]. One orthorhombic unit cell is shown, containing 4 Cs, 8 Cu and 12 halogen atoms.

shows that nonempirical hybrid functionals that depend on the dielectric properties of the material yield accurate optical spectra for $CsCu_2X_3$. This suggests that hybrid functionals are very well suited for calculating the optical properties in all-inorganic perovskites, and more generally for calculations with large unit cells and high-throughput computations.

This paper is organized as follows: in Sec. II we give an overview of the theoretical background, with an emphasis on the different TDDFT hybrid functionals. We also discuss computational details. The results for the optical spectra and excitonic properties of $CsCu_2X_3$ are presented in Sec. III. Section IV then gives our conclusions and an outlook.

II. THEORY AND COMPUTATIONAL DETAILS

A. A Brief Overview of Hybrid Functionals

In ground-state DFT, the central idea of hybrid functionals is to write the exchange-correlation (xc) energy functional as [43–47]

$$E_{\rm xc}^{\rm hybrid} = aE_{\rm x}^{\rm exact} + (1-a)E_{\rm x}^{\rm sl} + E_{\rm c}^{\rm sl}\,, \qquad (1)$$

where $E_{\rm x}^{\rm exact}$ is the exact nonlocal (Fock) exchange energy functional, and $E_{\rm x,c}^{\rm sl}$ are approximate (semi)local (sl) exchange and correlation functionals, respectively. $E_{\rm xc}^{\rm hybrid}$ contains a parameter a which mixes exact exchange with (semi)local exchange. There are hybrid functionals with two or more mixing parameters [46], but for simplicity we will not include them in our discussion. In practice, hybrid functionals are normally used within the so-called generalized Kohn-Sham approach [42].

One may distinguish different types of hybrid functionals. In *global* hybrids, the fraction a of exact exchange is a constant throughout the system. In *local* hybrids, the parameter a depends on position [71]. The *range-separated* hybrid functionals [72], by contrast, consider the xc interactions of long range and short range separately. The most popular way of doing this is by partitioning the Coulomb interaction as

$$\frac{1}{r} = \frac{\alpha+\beta{\rm erf}(\gamma r)}{r} + \frac{1-[\alpha+\beta{\rm erf}(\gamma r)]}{r}\,, \qquad (2)$$

where the first (long-range) term enters the Fock exchange, and the second (short-range) term enters the (semi)local exchange [73], or vice versa [74]. Typical examples for the global and range-separated hybrid functionals are PBE0 [47] (with simply $a = 0.25$) and HSE06 [48], respectively. Although the parameters in both functionals are determined empirically, PBE0 and HSE06, as well as other empirical hybrid functionals, have been widely used for periodic solids, mainly for the resulting improvement of band gaps [54, 56–60, 75]. The range separation parameters can also be determined (or "tuned") using certain exact conditions, which has been quite successful for molecules and molecular crystals [72, 76].

On the other hand, the ongoing effort to construct nonempirical hybrid functionals for solids has made remarkable progress. A class of dielectric-dependent hybrid functionals (DDHs) have been proposed [50–52, 58, 62], where the dielectric function is used to determine the parameters in Eqs. (1) or (2). Since the dielectric function can be calculated from the random phase approximation (RPA), the resulting hybrid functionals are made nonempirical. For solids with a finite gap, the screening of the long-range tail of the Coulomb interaction is proportional to the inverse of the static dielectric constant (ε_∞^{-1}). It is intuitive to identify the parameter a in Eq. (1) with ε_∞^{-1}, which directly leads to a global DDH. For range-separated DDHs [51, 52], using the same long-range limit of Coulomb interaction, one obtains $\alpha+\beta = \varepsilon_\infty^{-1}$. The only remaining parameter, the range-separation parameter γ, is then fitted to reproduce either the fundamental band gap or the finite-range dielectric function of the system. In addition, the parameters in both global and range-separated DDHs can be optimized via an iterated procedure to obtain a self-consistent dielectric constant (or dielectric function) [50, 67]. In the following, we refer to DDHs where the dielectric function is calculated using the RPA with (nonhybrid) DFT wave functions as *single-shot* hybrid functionals, analogous to the widely used single-shot G_0W_0 approach.

Applications of hybrid TDDFT for optical spectra in semiconductors and insulators have begun to emerge [70, 76–86]. For instance, Lewis *et al.* recently showed that range-separated hybrids with an empirical parameter agree well with GW+BSE results for gallium nitride with defects [84]. Furthermore, it was recently reported that DDHs yield band gaps of good accuracy for inorganic metal-halide perovskites [67]; this suggests that DDHs may be suitable for the optical properties of perovskites. We will see below that this is indeed the case.

B. Connection between BSE and hybrid functionals for excitons in solids

From the point of view of generalized (TD)DFT, hybrid functionals bridge the density-based (TD)DFT and the orbital-based many-body theory via a fraction of Fock exchange, while representing the N-electron wave function as a single Slater determinant with single-particle orbitals φ_i [41, 42]. For ground states, global DDHs connect to the static approximation of GW, known as the static COulomb Hole plus Screened EXchange (COHSEX) [50]. By adopting $a = \varepsilon_\infty^{-1}$, the long-ranged Fock exchange in Eq. (1) corresponds to the statically screened exchange (SEX) self-energy:

$$\begin{aligned}\Sigma_{\mathrm{SEX}}(\mathbf{r},\mathbf{r}') &= -\sum_{i=1}^{N}\varphi_i(\mathbf{r})\varphi_i^*(\mathbf{r}')W(\mathbf{r},\mathbf{r}') \\ &\approx -\varepsilon_\infty^{-1}\sum_{i=1}^{N}\frac{\varphi_i(\mathbf{r})\varphi_i^*(\mathbf{r}')}{|\mathbf{r}-\mathbf{r}'|}\,.\end{aligned} \tag{3}$$

Here, the screened Coulomb potential W is given by

$$W(\mathbf{r},\mathbf{r}') = \int d\mathbf{r}''\,\frac{\varepsilon^{-1}(\mathbf{r},\mathbf{r}')}{|\mathbf{r}'-\mathbf{r}'|}\,. \tag{4}$$

For the range-separated DDHs, the error function $\mathrm{erf}(\gamma|\mathbf{r}-\mathbf{r}'|)$ offers a good model for the dielectric function $\varepsilon^{-1}(\mathbf{r},\mathbf{r}')$ in 3D solids. In reciprocal space, ε^{-1} thus becomes [51, 52]

$$\varepsilon^{-1}(q) = \varepsilon_\infty^{-1} + (1-\varepsilon_\infty^{-1})(1-e^{-q^2/4\gamma^2})\,. \tag{5}$$

Thus, $W(\mathbf{r},\mathbf{r}')$ can be evaluated using model dielectric functions in Eq. (5), thereby connecting range-separated DDHs to the COHSEX via Eq. (3) [51, 52].

For excited states, one finds that generalized TDDFT is connected to the BSE in a similar way. Taking the Tamm-Dancoff approximation with momentum transfer $\mathbf{q}=0$ [87–89], the BSE can be simply expressed as

$$\left[(E_{c,\mathbf{k}}-E_{v,\mathbf{k}'})\delta_{vv'}\delta_{cc'}\delta_{\mathbf{k}\mathbf{k}'} + K^{\mathrm{BSE}}_{cv\mathbf{k},c'v'\mathbf{k}'}\right]\mathbf{Y}_n = \omega_n\mathbf{Y}_n. \tag{6}$$

Here, v denotes occupied valence bands, c denotes unoccupied conduction bands, the $E_\mathbf{k}$ are QP energies, $\mathbf{Y}_n$ are the nth eigenvectors, and ω_n is the nth excitation energy. Equation (6) features the coupling matrix (or BSE kernel) $K^{\mathrm{BSE}} = K^{\mathrm{d}} + K^{\mathrm{x}}$. The first part, K^{d}, is the direct interaction, corresponding to the Hartree part in TDDFT. The second part is the screened exchange kernel,

$$\begin{aligned}K^{\mathrm{x}}(\mathbf{q},\omega) = \frac{2}{V_{\mathrm{cell}}}\sum_{\mathbf{G},\mathbf{G}'} & W_{\mathbf{G},\mathbf{G}'}(\mathbf{q},\omega)\delta_{\mathbf{q},\mathbf{k}-\mathbf{k}'} \\ & \times\langle c\mathbf{k}|\,e^{i(\mathbf{q}+\mathbf{G})\mathbf{r}}\,|c'\mathbf{k}'\rangle\,\langle v'\mathbf{k}'|\,e^{-i(\mathbf{q}+\mathbf{G}')\mathbf{r}}\,|v\mathbf{k}\rangle\,.\end{aligned} \tag{7}$$

Here, $W_{\mathbf{G},\mathbf{G}'}(\mathbf{q},\omega)$ is the dynamically screened Coulomb interaction in reciprocal space,

$$W_{\mathbf{G},\mathbf{G}'}(\mathbf{q},\omega) = -\frac{4\pi\varepsilon^{-1}_{\mathbf{G},\mathbf{G}'}(\mathbf{q},\omega)}{|\mathbf{q}+\mathbf{G}||\mathbf{q}+\mathbf{G}'|}, \tag{8}$$

where in standard BSE $\varepsilon^{-1}_{\mathbf{G},\mathbf{G}'}(\mathbf{q},\omega)$ is obtained via RPA, as mentioned before. For most practical BSE calculations, the frequency dependence of the dielectric function is ignored, i.e., one uses $\varepsilon^{-1}_{\mathbf{G},\mathbf{G}'}(\mathbf{q},\omega=0)$ [90–92].

Similar to the approximations for GW, one can replace the RPA dielectric function by a model dielectric function $\varepsilon_{\mathrm{m}}^{-1}(q)$ or just a simple parameter, both of them diagonal in the reciprocal lattice vectors $\mathbf{G},\mathbf{G}'$:

$$\varepsilon^{-1}_{\mathbf{G},\mathbf{G}'}(\mathbf{q},0) \longrightarrow \begin{cases} \varepsilon_{\mathrm{m}}^{-1}(q)\delta_{\mathbf{G},\mathbf{G}'} & \text{(m-BSE)} \\ a\delta_{\mathbf{G},\mathbf{G}'} & \text{(SXX).}\end{cases} \tag{9}$$

Here, m-BSE stands for BSE with a model dielectric function, and SXX stands for screened exact exchange [70, 85]. If $a=1$, SXX reduces to time-dependent Hartree-Fock.

Combining SXX and (semi)local exchange and correlation thus leads to a hybrid kernel for generalized TDDFT, analogous to Eq. (1):

$$K_{\mathrm{xc}}^{\mathrm{hybrid1}} = K^{\mathrm{SXX}} + (1-a)K_{\mathrm{x}}^{\mathrm{sl}} + K_{\mathrm{c}}^{\mathrm{sl}}\,, \tag{10}$$

where $K_{\mathrm{x}}^{\mathrm{sl}}$ and $K_{\mathrm{c}}^{\mathrm{sl}}$ are the adiabatic (semi)local exchange and correlation kernels, respectively. Replacing the BSE kernel K^{BSE} with the hybrid kernel in Eq. (6) defines our generalized TDDFT scheme for optical excitations in solids. In the following, we choose the adiabatic local-density approximation (ALDA) kernels to construct the hybrid kernel, i.e., we set

$$\begin{aligned}K_{\mathrm{x,c}}^{\mathrm{sl}}(\mathbf{q}) = \frac{2}{V_{\mathrm{cell}}}\lim_{\mathbf{q}\to 0}\sum_{\mathbf{G},\mathbf{G}'} & f_{\mathrm{x,c},\mathbf{G}\mathbf{G}'}^{\mathrm{ALDA}}(\mathbf{q}) \\ & \times\langle c\mathbf{k}|\,e^{i(\mathbf{q}+\mathbf{G})\mathbf{r}}\,|v\mathbf{k}\rangle\,\langle v'\mathbf{k}'|\,e^{-i(\mathbf{q}+\mathbf{G}')\mathbf{r}}\,|c'\mathbf{k}'\rangle\,,\end{aligned} \tag{11}$$

where $f_{\mathrm{x,c},\mathbf{G}\mathbf{G}'}^{\mathrm{ALDA}}(\mathbf{q})$ are the local frequency-independent exchange and correlation kernels in ALDA [38, 93].

The expressions Eq. (1) and Eq. (10) are constructed following the standard TDDFT hybrid functional form. However, in extended many-body systems, not only the exchange but also the correlation is subject to dielectric screening; this can, for instance, be explicitly seen in the COH part of the COHSEX approximation for the QP self-energy [94]. Hence, the (semi)local correlation energy, $E_{\mathrm{c}}^{\mathrm{sl}}$, should also be screened in order to avoid overcounting of correlation. This leads us to define a second form of hybrid functional,

$$K_{\mathrm{xc}}^{\mathrm{hybrid2}} = K^{\mathrm{SXX}} + (1-a)K_{\mathrm{xc}}^{\mathrm{sl}}\,, \tag{12}$$

which was already proposed earlier, and was found to compare well with the BSE [70].

In the following, we will assess three hybrid kernels based on the definitions in Eq. (10) and Eq. (12). The first one, LDA0, is built as a traditional empirical hybrid functional in analogy with PBE0 [47], by setting $a=0.25$ in Eq. (10). The other two, DDH1 and DDH2, are built by identifying a with the RPA inverse dielectric constant $\varepsilon_{0,0}^{-1}$ in Eqs. (10) and (12), respectively. A detailed comparison of the hybrid kernels will be given in Section III B.

C. Computational Details

For $CsCu_2X_3$, calculating the crystal structure with relaxed atomic positions using pure DFT, hybrid functionals or even *GW* can lead to errors compared to the experimental lattice constants and geometries [69], which affects the calculated band gaps in uncontrolled ways. To eliminate this problem, we simply adopted the experimental crystal structures, lattice constants and atomic positions for all three materials $CsCu_2X_3$ [18].

To calculate Kohn-Sham band structures, we used the LDA and PBE [95] functionals in the Quantum Espresso package [96], based on the plane-wave basis with cutoff energy of 85 Ry. We adopted optimized norm-conserving Vanderbilt pseudopotentials [97, 98] for all the elements with both LDA and PBE, with the exception of using the Troullier-Martins pseudopotential for Cs with LDA [99]. The validation of this mixed pseudopotential setting is provided by comparing the band structures from LDA and PBE functionals (see Supplemental Material [100]).

Starting from the Kohn-Sham band structures, we then used the Yambo code [101] to obtain dielectric functions and QP band structures. The RPA dielectric functions were calculated with 300 bands and 600 **G**-vectors. For the QP band structures, we used the single-shot G_0W_0 scheme with at least 400 bands. Although the dielectric function, as well as GW+BSE, are introduced within the static approximation, the ω-dependent dynamic effects of the dielectric screening may have a nonnegligible influence on the electron dynamics [102–105]. In this work, the generalized-plasmon-pole model [103] was applied to account for the dynamical effects. Thanks to the flexible definition of K^{SXX}, it is compatible with dynamically corrected RPA inverse dielectric constants ($\varepsilon^{-1}_{0,0}$). In the following, such definition of $\varepsilon^{-1}_{0,0}$ is used, including building the DDHs, unless explicitly stated otherwise.

A double-grid was adopted, which includes a $4 \times 3 \times 8$ Γ-centered **k**-point mesh plus 3000 random interpolated **k**-points. This enabled us to apply the random integration method, as well as an inversion solver for the BSE-type equations [101, 106]. To build the BSE-type kernels, we used 56 valence bands and 20 conduction bands for $CsCu_2Cl_3$. The corresponding numbers of valence and conduction bands are 44 and 10 for $CsCu_2Br_3$ and 18 and 14 for $CsCu_2I_3$. A broadening of 0.1 eV was used to calculate the optical spectra.

We performed convergence tests regarding the **k**-point grid and number of bands included in the G_0W_0 calculations, and found that the choices detailed above lead to well-converged results for band gaps, exciton binding energies and optical spectra (see Supplemental Material [100]).

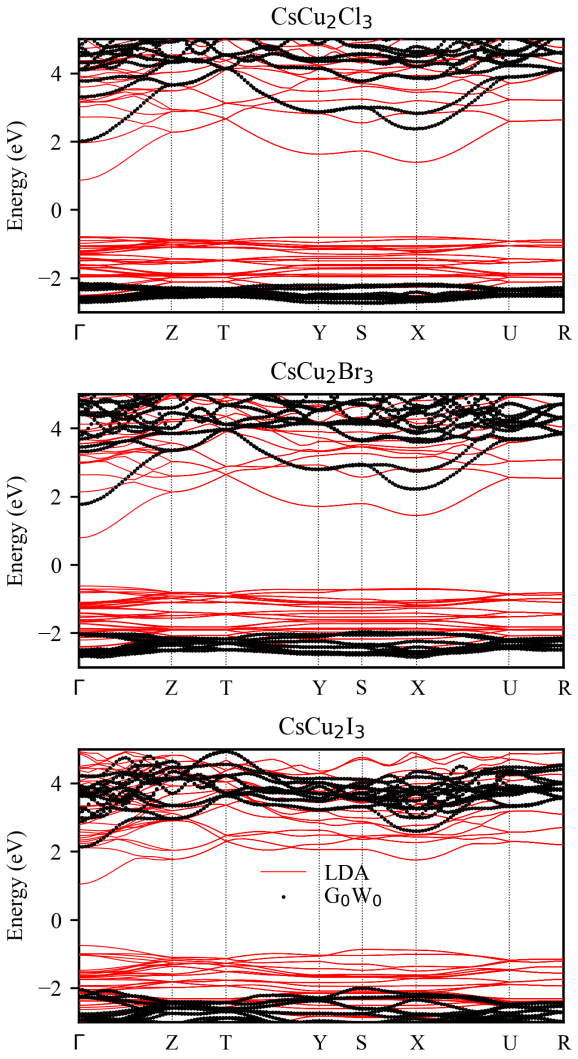

FIG. 2. Band structures of $CsCu_2X_3$, calculated with LDA and G_0W_0@LDA.

III. RESULTS AND DISCUSSION

A. Band Structures and band gaps

We begin by comparing the band structures of the Cs-Cu halides calculated with different approaches, namely, Kohn-Sham band structures from LDA and PBE, and single-shot *GW* band structures on top of LDA and PBE (G_0W_0@LDA and G_0W_0@PBE).

Figure 2 shows the band structures of $CsCu_2X_3$ obtained by LDA and G_0W_0@LDA. As expected, there are important differences, most notably a pronounced opening up of the band gaps caused by the QP corrections. Along with the enlarged band gaps, the conduction bands in all three materials are significantly altered in G_0W_0, especially around the X point. In addition, the valence bands are strongly affected as well: for the case of $CsCu_2I_3$, this is most apparent for the highest occu-

TABLE I. Band gaps of $CsCu_2X_3$, calculated with DFT and G_0W_0. All energies are in eV.

	LDA	G_0W_0@LDA	PBE	G_0W_0@PBE	PBE0[a]
$CsCu_2Cl_3$	1.65	4.20	1.78	3.92	4.29
$CsCu_2Br_3$	1.40	3.63	1.59	3.47	3.88
$CsCu_2I_3$	1.79	4.03	1.98	3.83	3.93

[a] from Ref. [69]

pied valence bands between the Γ and Z points, as well as for the valence bands around the S point. Overall, these differences in the band structures suggest that a simple scissors operator approach (which would not change the shape of the LDA bands, just shift them rigidly) is not sufficiently accurate for calculating the optical properties in these materials.

In the Supplemental Material [100], we show that the band structures obtained by LDA and G_0W_0@LDA are very similar to the PBE and G_0W_0@PBE band structures, respectively, except for some differences of the band gaps, see below. In view of this, will use the G_0W_0@LDA band structures as input for the BSE and TDDFT calculations of the optical spectra in the following sections.

The calculated band gaps are listed in Table I, together with PBE0 results from Ref. [69]. As already pointed out, both LDA and PBE gaps are significantly smaller than the corresponding G_0W_0 gaps. Unfortunately, no experimental results for the QP gaps E_g^{QP} in $CsCu_2X_3$ are available. In Section III B we will discuss the optical gaps E_g^{opt} in some detail; due to excitonic effects, the optical gap is a lower limit to the QP gap. As seen in Table II, the experimental optical gaps are on the order of 3.8 eV [18, 19], which clearly shows that LDA and PBE dramatically underestimate the QP gaps.

After QP correction, the G_0W_0 gaps are drastically enhanced over the corresponding Kohn-Sham gaps, by about 2 eV. While LDA gives smaller band gaps than PBE, the G_0W_0@LDA gap is larger than the G_0W_0@PBE gap for all materials under study. We note that the band gaps obtained with PBE0 [69] are comparable to G_0W_0, which indicates the capability of hybrid functionals for predicting band gaps in perovskites.

We also implemented the DDH1 and DDH2 functionals to calculate the band gaps; to reduce computational cost, the calculations were performed single-shot rather than self-consistently. It is found that single-shot DDH1 and DDH2 tend to somewhat overestimate the band gap compared to G_0W_0. These results are discussed in more detail in the Supplemental Material [100].

A special case here is $CsCu_2Br_3$, where the G_0W_0 gaps are smaller than the experimental optical gap [18]. Possible explanations for this underestimation could be missing core electron effects [67] or G_0W_0 starting point dependence [107, 108] (see Supplemental Material [100] for further discussion). On the other hand, the PBE0 gap is better compatible with the experimental E_g^{opt}; however, the PBE0 calculation was done with the relaxed lattice structure rather than the experimental geometry [69], and the band gap is sensitive to changes of the atomic positions.

TABLE II. Excitonic binding energies (E_b, in meV) calculated using BSE, RPA inverse dielectric constants ($\varepsilon^{-1}_{0,0}$) along different directions, as well as calculated and experimental (in parentheses) optical gaps (E_g^{opt}, in eV).

	[100]		[010]		[001]		
	E_b	$\varepsilon^{-1}_{0,0}$	E_b	$\varepsilon^{-1}_{0,0}$	E_b	$\varepsilon^{-1}_{0,0}$	E_g^{opt}
$CsCu_2Cl_3$	611	0.35	425	0.37	701	0.31	3.50 (3.89[a])
$CsCu_2Br_3$	321	0.30	120	0.31	219	0.28	3.32 (3.89[a])
$CsCu_2I_3$	156	0.26	51	0.26	32	0.25	3.86 (3.71[a], 3.78[b])

[a] from Ref. [18]
[b] from Ref. [19]

B. Optical spectra via the BSE

We now discuss the optical properties of the Cs-Cu halides, beginning with the G_0W_0+BSE results. We compare the spectra associated with light polarization along the [100], [010], and [001] directions, which highlights the anisotropic, quasi-1D structure of $CsCu_2X_3$, see Fig. 1. The excitonic biding energies are obtained via the standard definition, i.e. $E_b = E_g^{QP} - E_{exc}$, where E_{exc} is the excitation energy of the lowest bright exciton along corresponding direction. The calculated excitonic binding energies are given in Table II, and the G_0W_0+RPA and G_0W_0+BSE optical spectra (imaginary part of the dielectric function) are displayed in Fig. 3.

As shown in Table II, the E_b in $CsCu_2Cl_3$ along [100], [010], and [001] are 611 meV, 425 meV, and 701 meV, respectively, which is almost ten times larger than in the widely studied lead halide perovskites, $CsPbX_3$ and $CH_3NH_3PbX_3$ [26–30]. These large binding energies are associated with distinct excitonic optical absorption peaks that are separated from the continuum part of the spectrum, as observed in the upper panel of Fig. 3. In the BSE optical spectra, strong absorption peaks appear below the QP band gap for all three directions; these peaks are completely missing in RPA.

Comparing the E_b of the three materials in Table II, one finds that the excitons become more and more weakly bound going from X = Cl to Br and then to I. From Fig. 3 we see that the excitonic peaks move closer and closer to the QP band gaps for $CsCu_2Br_3$ and $CsCu_2I_3$. In particular, there is no longer a separate excitonic peak along [010] and [001] for $CsCu_2I_3$. The corresponding E_b are 51 meV and 32 meV, which is of the same magnitude as E_b in $CsPbX_3$ and $CH_3NH_3PbX_3$, and similar to those in many binary semiconductors such as GaN or ZnO. In all of those cases, one observes that the excitonic peaks merge with the onset of the absorption continuum above the QP gap.

The main reason for the decreasing E_b from $CsCu_2Cl_3$ to $CsCu_2I_3$ is the increasing dielectric screening. As

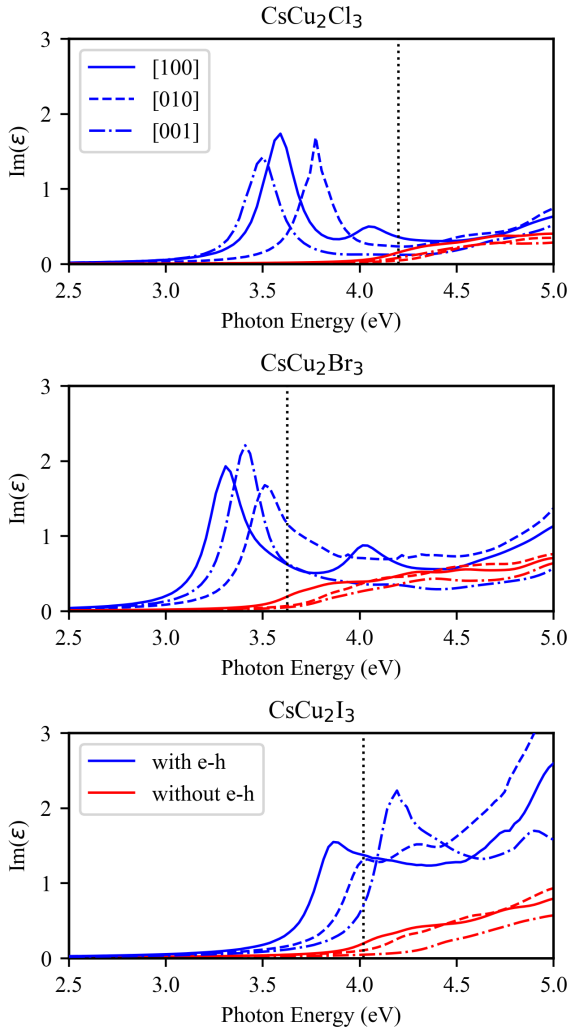

FIG. 3. Optical spectra Im(ε) calculated with G_0W_0+RPA (red lines) and G_0W_0+BSE (blue lines). The vertical dotted lines indicate the positions of the G_0W_0@LDA band gaps.

shown in Table II, a decreasing trend of RPA $\varepsilon^{-1}_{0,0}$ is found from $CsCu_2Cl_3$ to $CsCu_2I_3$ for each direction. This reflects an enhancement of the overall dielectric screening as the X ions evolve from Cl to I, which is also found in $CsBX_3$ (B = Ge, Sn, Pb and X = Cl, Br, I) [67]. Moreover, the experimentally measured binding energies of trapped excitons show the same trend [18], though they differ from the E_b of free excitons that are considered here.

There is a strong anisotropy of the excitons in $CsCu_2X_3$: E_b along [100] is significantly larger than that along [010] for each $CsCu_2X_3$. On the other hand, the relation of the [001] exciton to the [100] and [010] excitons changes with X: E_b along [001] is the largest of the three in $CsCu_2Cl_3$, but then becomes the intermediate and the smallest one in $CsCu_2Br_3$ and $CsCu_2I_3$, respectively. This change can also be nicely seen for the [001] absorption peak in the optical spectra in Fig. 3. These

TABLE III. Excitonic binding energies (E_b, in meV) along [111], calculated using BSE and hybrid functionals, and RPA inverse dielectric constants ($\varepsilon^{-1}_{0,0}$).

	$\varepsilon^{-1}_{0,0}$	E_b			
		BSE	LDA0	DDH1	DDH2
$CsCu_2Cl_3$	0.343	701	423	682	682
$CsCu_2Br_3$	0.298	321	227	316	317
$CsCu_2I_3$	0.254	156	150	151	151

anisotropy effects cannot be explained by the macroscopic dielectric screening; for example, in $CsCu_2Cl_3$, E_b along [100] is smaller than along [001], but $\varepsilon^{-1}_{0,0}$ along [100] is larger than along [001]. A better explanation would be the strong local-field effects in these ionic crystals.

Besides the absence of distinct excitonic peaks below the band gap, there are additional differences between the BSE and RPA spectra. First, the continuum absorption above the band gap is enhanced by including electron-hole interactions, especially for $CsCu_2I_3$. Secondly, the RPA spectrum in each material always has the highest absorption edge along the [001] direction. In other words, the change of the absorption edges along [001] discussed in last paragraph is not observed in RPA. Clearly, the RPA is inadequate for calculating the optical properties of $CsCu_2X_3$.

Lastly, in the rightmost column of Table II we compare the calculated optical gap with experiment [18, 19]. The optical gap is defined as $E_g^{opt} = E_g^{QP} - E_b$, where E_g^{QP} is here the fundamental G_0W_0@LDA band gap and E_b is the binding energy of the lowest energy exciton among all three directions. The calculated E_g^{opt} of $CsCu_2I_3$ is in good agreement with experiment, but it is somewhat too low for $CsCu_2Cl_3$ and $CsCu_2Br_3$ (by 0.39 and 0.57 eV, respectively). These deviations may have multiple sources. The fundamental gaps of both materials could be underestimated, as we have mentioned above for $CsCu_2Br_3$. Furthermore, the exciton binding energies are likely overestimated by G_0W_0+BSE, which is also observed for the strongly bound excitons in LiF [70, 90, 91]. To address this issue, one could apply self-consistent G_0W_0 with vertex correction, as well as an all-electron implementation; this is, however, beyond the scope of this work.

C. Performance of the Hybrid Functionals

We now compare the optical properties obtained by different hybrid functionals with BSE. Rather than discussing the [100], [010], and [001] spectra as in Section III B, we here only consider the spectra along [111], which can be viewed as averaging over the crystalline anisotropy. All calculated binding energies of the lowest energy excitons are listed in Table III, and the optical spectra are plotted in Fig. 4.

We first point out that the BSE E_b along [111] in Table III are close to or the same as the largest E_b in Table II for each material. The slight enhancement of E_b

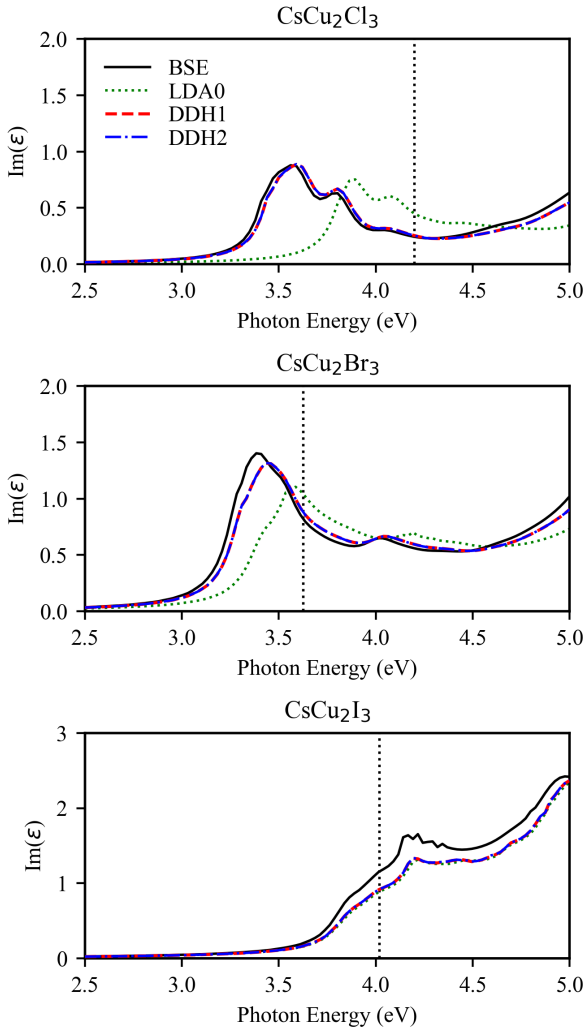

FIG. 4. Optical spectra Im(ε) along [111], calculated G_0W_0+BSE and hybrid functionals. The vertical dotted lines indicate the positions of the G_0W_0@LDA band gaps.

for $CsCu_2Cl_3$ is because $\varepsilon^{-1}_{0,0}$ is larger along [111] than along [001]. The $\varepsilon^{-1}_{0,0}$ along [111] is in fact close to or the same as $\varepsilon^{-1}_{0,0}$ along [100] for each material, which indicates a dominant role played by the dielectric constant along [100] in these anisotropic materials. We then use the $\varepsilon^{-1}_{0,0}$ in Table III as the prefactors of Fock exchange in the DDH1 and DDH2 functionals.

For all three materials, LDA0 underestimates E_b compared to BSE. The LDA0 produces an error as large as 40% for $CsCu_2Cl_3$. This can be clearly seen in the optical spectra in Fig. 4, where the LDA0 spectrum is significantly blueshifted for $CsCu_2Cl_3$. The reason for the substantial LDA0 errors is the improper $a = 0.25$, which leads to an overscreened Coulomb interaction. The error caused by the empirical a becomes less severe going from $CsCu_2Cl_3$ to $CsCu_2I_3$. As $\varepsilon^{-1}_{0,0}$ comes closer to $a = 0.25$, the LDA0 error of E_b decreases to 29% for $CsCu_2Br_3$ and to 3% for $CsCu_2I_3$.

For the hybrid functionals DDH1 and DDH1 we have $a = \varepsilon^{-1}_{0,0}$, and E_b deviates less than 3.5% from BSE. As shown in Fig. 4, the DDH spectra of $CsCu_2Cl_3$ are almost identical to the BSE spectra, apart from a tiny blueshift. For $CsCu_2Br_3$, the DDHs reproduce the slight shoulder at about 3.3 eV. However, both DDHs underestimate the height of the dominant peak at about 3.4 eV, and shift it to about 3.5 eV. Comparing with the spectra in Fig. 3, we conclude that this peak arises from the excitonic effects along [001]. Similar DDH results are found for $CsCu_2I_3$: E_b of the lowest energy exciton is very well reproduced, but the strength of the excitonic effects along [001] is somewhat underestimated. This suggests that the local-field effects of the excitons in $CsCu_2X_3$ may not be fully captured by DDH1 and DDH2. We attribute this to the global prefactor of the Fock exchange; using range-separated DDH functionals might improve the description. Nevertheless, it is evident that the nonempirical global DDHs are able to predict E_b and the optical spectra of $CsCu_2X_3$ with very good accuracy (using BSE as reference).

Finally, we point out the very close agreement between DDH1 and DDH2. From Eqs. (10) and (12), the difference between DDH1 and DDH2 is aE_c. For $CsCu_2X_3$, a is in the range of 0.25-0.35. In weakly correlated materials such as those considered here, correlation effects are typically an order of magnitude smaller than exchange effects. Thus, aE_c does not make much of a difference for the optical properties of $CsCu_2X_3$. However, we emphasize that there is no guarantee that the two functionals DDH1 and DDH2 perform the same way in other systems, especially materials with small dielectric constant (larger a) or stronger correlation. In such cases, it might turn out that other forms of hybrid functionals, perhaps involving additional parameters, are preferable.

IV. CONCLUSIONS

In this work, we have shown that hybrid TDDFT is a very promising alternative to the BSE for calculating the optical properties of semiconducting and insulating materials. To demonstrate this, we chose a class of perovskite materials, the Cs-Cu halides, with a relatively complex structure containing 24 atoms per unit cell. These materials have a quasi-1D structure and strong excitonic features, giving rise to light emission properties with potential for technological application.

Calculating the optical absorption spectrum of a material is a two-step process. First, the equilibrium band structure must be obtained, and then the spectrum is calculated using linear response. In the many-body approach, the QP band structure is calculated using GW, followed by the BSE. TDDFT instead takes Kohn-Sham band structures as input. Generalized TDDFT, using hybrid functionals, can be viewed as a bridge between these two approaches.

Strictly speaking, the consistent way to implement generalized TDDFT is to calculate the band structure and the spectrum using the same hybrid functional. In this paper, we instead chose to use the same G_0W_0 band structures as input for both TDDFT and the BSE, because our focus was not on the performance of hybrid functionals for the band structure (which has been widely studied in the literature), but rather on the performance for calculating optical spectra with prominent excitonic effects. Using different input band structures would have made a direct comparison difficult. Furthermore, as shown in the Supplemental Material [100], using hybrid band structures together with hybrid TDDFT does not lead to better optical gaps than G_0W_0+BSE.

Here, we considered two different types of hybrid functionals: LDA0, which has a fixed, material-independent mixing parameter, and DDH1 and DDH2, with a mixing parameter dependent on the dielectric constant of the material. The main finding is that only the dielectric-dependent hybrids can properly account for the screening effects, and they do so extremely well: both DDH1 and DDH2 (which slightly differ in the way in which local exchange-correlation is mixed with exact exchange) produce optical spectra that are very close to the BSE.

The computational cost of hybrid TDDFT can be significantly lower than that of the BSE; in a previous study [70], substantial CPU time reductions were achieved, depending on details of the implementation. Since those cost savings come at practically no loss of accuracy as we have seen here, this clearly shows that hybrid TDDFT should become the method of choice for calculating excited-state properties of complex materials.

Dielectric-dependent hybrid functionals clearly warrant further study. Tests for additional classes of materials, including low-dimensional structures, are necessary to find the optimal form of hybrid functionals for extended solids. In particular, a systematic comparison of dielectric-dependent hybrids with and without range separation would be of interest. Another intriguing question is how dynamical screening effects, which are neglected in most applications of the BSE [109, 110], would carry over into the framework of generalized TDDFT.

ACKNOWLEDGMENTS

This work was supported by NSF grant No. DMR-1810922. The computation for this work was performed on the high performance computing infrastructure provided by Research Computing Support Services at the University of Missouri-Columbia.

[1] M. D. Smith and H. I. Karunadasa, White-light emission from layered halide perovskites, Acc. Chem. Res. **51**, 619 (2018).

[2] E. R. Dohner, A. Jaffe, L. R. Bradshaw, and H. I. Karunadasa, Intrinsic white-light emission from layered hybrid perovskites, J. Am. Chem. Soc. **136**, 13154 (2014).

[3] X. Gong, O. Voznyy, A. Jain, W. Liu, R. Sabatini, Z. Piontkowski, G. Walters, G. Bappi, S. Nokhrin, O. Bushuyev, M. Yuan, R. Comin, D. McCamant, S. O. Kelley, and E. H. Sargent, Electron–phonon interaction in efficient perovskite blue emitters, Nat. Mater. **17**, 550 (2018).

[4] Z. Yuan, C. Zhou, Y. Tian, Y. Shu, J. Messier, J. C. Wang, L. J. van de Burgt, K. Kountouriotis, Y. Xin, E. Holt, K. Schanze, R. Clark, T. Siegrist, and B. Ma, One-dimensional organic lead halide perovskites with efficient bluish white-light emission, Nat. Commun. **8**, 14051 (2017).

[5] G. Wu, C. Zhou, W. Ming, D. Han, S. Chen, D. Yang, T. Besara, J. Neu, T. Siegrist, M.-H. Du, B. Ma, and A. Dong, A one-dimensional organic lead chloride hybrid with excitation-dependent broadband emissions, ACS Energy Lett. **3**, 1443 (2018).

[6] C. Zhou, H. Lin, M. Worku, J. Neu, Y. Zhou, Y. Tian, S. Lee, P. Djurovich, T. Siegrist, and B. Ma, Blue emitting single crystalline assembly of metal halide clusters, J. Am. Chem. Soc. **140**, 13181 (2018).

[7] M. I. Saidaminov, J. Almutlaq, S. Sarmah, I. Dursun, A. A. Zhumekenov, R. Begum, J. Pan, N. Cho, O. F. Mohammed, and O. M. Bakr, Pure Cs_4PbBr_6: Highly luminescent zero-dimensional perovskite solids, ACS Energy Lett. **1**, 840 (2016).

[8] T. Li, X. Mo, C. Peng, Q. Lu, C. Qi, X. Tao, Y. Ouyang, and Y. Zhou, Distinct green electroluminescence from lead-free $CsCuBr_2$ halide micro-crosses, Chem. Commun. **55**, 4554 (2019).

[9] E. P. Booker, J. T. Griffiths, L. Eyre, C. Ducati, N. C. Greenham, and N. J. L. K. Davis, Synthesis, characterization, and morphological control of Cs_2CuCl_4 nanocrystals, J. Phys. Chem. C **123**, 16951 (2019).

[10] L. Etgar, The merit of perovskite's dimensionality; can this replace the 3D halide perovskite?, Energy Environ. Sci. **11**, 234 (2018).

[11] Q. Fu, X. Tang, B. Huang, T. Hu, L. Tan, L. Chen, and Y. Chen, Recent progress on the long-term stability of perovskite solar cells, Adv. Sci. **5**, 1700387 (2018).

[12] T. Jun, K. Sim, S. Iimura, M. Sasase, H. Kamioka, J. Kim, and H. Hosono, Lead-free highly efficient blue-emitting $Cs_3Cu_2I_5$ with 0D electronic structure, Adv. Mater. **30**, 1804547 (2018).

[13] P. Cheng, L. Sun, L. Feng, S. Yang, Y. Yang, D. Zheng, Y. Zhao, Y. Sang, R. Zhang, D. Wei, W. Deng, and K. Han, Colloidal synthesis and optical properties of all-inorganic low-dimensional cesium copper halide nanocrystals, Angew. Chem. **131**, 16233 (2019).

[14] P. Vashishtha, G. V. Nutan, B. E. Griffith, Y. Fang, D. Giovanni, M. Jagadeeswararao, T. C. Sum, N. Mathews, S. G. Mhaisalkar, J. V. Hanna, and T. White, Cesium copper iodide tailored nanoplates and nanorods for blue, yellow, and white emission, Chem. Mater. **31**, 9003 (2019).

[15] Y. Li, Z. Shi, W. Liang, L. Wang, S. Li, F. Zhang, Z. Ma, Y. Wang, Y. Tian, D. Wu, X. Li, Y. Zhang, C. Shan, and X. Fang, Highly stable and spectrum-selective ultraviolet photodetectors based on lead-free copper-based perovskites, Mater. Horiz. **7**, 530 (2020).

[16] B. Yang, L. Yin, G. Niu, J.-H. Yuan, K.-H. Xue, Z. Tan, X.-S. Miao, M. Niu, X. Du, H. Song, E. Lifshitz, and J. Tang, Lead-free halide Rb_2CuBr_3 as sensitive X-ray scintillator, Adv. Mater. **31**, 1904711 (2019).

[17] T. D. Creason, A. Yangui, R. Roccanova, A. Strom, M.-H. Du, and B. Saparov, Rb_2CuBr_3 (X = Cl, Br): 1D all-inorganic copper halides with ultrabright blue emission and up-conversion photoluminescence, Adv. Opt. Mater. **8**, 1901338 (2019).

[18] R. Roccanova, A. Yangui, G. Seo, T. D. Creason, Y. Wu, D. Y. Kim, M.-H. Du, and B. Saparov, Bright luminescence from nontoxic $CsCu_2X_3$ (X = Cl, Br, I), ACS Mater. Lett. **1**, 459 (2019).

[19] R. Lin, Q. Guo, Q. Zhu, Y. Zhu, W. Zheng, and F. Huang, All-inorganic $CsCu_2I_3$ single crystal with high-PLQY ($\approx$ 15.7 %) intrinsic white-light emission via strongly localized 1D excitonic recombination, Adv. Mater. **31**, 1905079 (2019).

[20] Q. Li, Z. Chen, B. Yang, L. Tan, B. Xu, J. Han, Y. Zhao, and J. Tang, Pressure-induced remarkable enhancement of self-trapped exciton emission in one-dimensional $CsCu_2I_3$ with tetrahedral units, J. Am. Chem. Soc. **142**, 1786– (2020).

[21] J. Luo, X. Wang, S. Li, J. Liu, Y. Guo, G. Niu, L. Yao, Y. Fu, L. Gao, Q. Dong, C. Zhao, M. Leng, F. Ma, W. Liang, L. Wang, S. Jin, J. Han, L. Zhang, J. Etheridge, J. Wang, Y. Yan, E. H. Sargent, and J. Tang, Efficient and stable emission of warm-white light from lead-free halide double perovskites, Nature **563**, 541 (2018).

[22] S. Li, J. Luo, J. Liu, and J. Tang, Self-trapped excitons in all-inorganic halide perovskites: Fundamentals, status, and potential applications, J. Phys. Chem. Lett. **10**, 1999 (2019).

[23] L. Lian, M. Zheng, P. Zhang, Z. Zheng, K. Du, W. Lei, J. Gao, G. Niu, D. Zhang, T. Zhai, S. Jin, J. Tang, X. Zhang, and J. Zhang, Photophysics in $Cs_3Cu_2X_5$ (X=Cl, Br, I): Highly luminescent self-trapped excitons from local structure symmetrization, Chem. Mater. **5**, 3462– (2020).

[24] T. Hu, M. D. Smith, E. R. Dohner, M.-J. Sher, X. Wu, M. T. Trinh, A. Fisher, J. Corbett, X. Y. Zhu, H. I. Karunadasa, and A. M. Lindenberg, Mechanism for broadband white-light emission from two-dimensional (110) hybrid perovskites, J. Phys. Chem. Lett. **7**, 2258 (2016).

[25] D. Han, H. Shi, W. Ming, C. Zhou, B. Ma, B. Saparov, Y.-Z. Ma, S. Chen, and M.-H. Du, Unraveling luminescence mechanisms in zero-dimensional halide perovskites, J. Mater. Chem. C **6**, 6398 (2018).

[26] A. Miyata, A. Mitioglu, P. Plochocka, O. Portugall, J. T.-W. Wang, S. D. Stranks, H. J. Snaith, and R. J. Nicholas, Direct measurement of the exciton binding energy and effective masses for charge carriers in organic-inorganic tri-halide perovskites, Nat. Phys. **11**, 582 (2015).

[27] G. R. Yettapu, D. Talukdar, S. Sarkar, A. Swarnkar, A. Nag, P. Ghosh, and P. Mandal, Terahertz conductivity within colloidal $CsPbBr_3$ perovskite nanocrystals: Remarkably high carrier mobilities and large diffusion lengths, Nano Lett. **16**, 4838 (2016).

[28] J. Li, X. Yuan, P. Jing, J. Li, M. Wei, J. Hua, J. Zhao, and L. Tian, Temperature-dependent photoluminescence of inorganic perovskite nanocrystal films, RSC Adv. **6**, 78311 (2016).

[29] M. Bokdam, T. Sander, A. Stroppa, S. Picozzi, D. D. Sarma, C. Franchini, and G. Kresse, Role of Polar Phonons in the Photo Excited State of Metal Halide Perovskites, Sci. Rep. **6**, 28618 (2016).

[30] J. Leveillee and A. Schleife, Free-electron effects on the optical absorption of the hybrid perovskite $CH_3NH_3PbI_3$ from first principles, Phys. Rev. B **100**, 035205 (2019).

[31] L. Reining, The GW approximation: content, successes and limitations, WIREs Comput. Mol. Sci. **8**, e1344 (2018).

[32] M. Rohlfing and S. G. Louie, Electron-hole excitations and optical spectra from first principles, Phys. Rev. B **62**, 4927 (2000).

[33] R. M. Martin, L. Reining, and D. M. Ceperley, *Interacting Electrons: Theory and Computational Approaches* (Cambridge University Press, Cambridge, 2016).

[34] X. Leng, F. Jin, M. Wei, and Y. Ma, GW method and Bethe-Salpeter equation for calculating electronic excitations, WIREs Comput. Mol. Sci. **6**, 532 (2016).

[35] E. Runge and E. K. U. Gross, Density-functional theory for time-dependent systems, Phys. Rev. Lett. **52**, 997 (1984).

[36] G. Onida, L. Reining, and A. Rubio, Electronic excitations: density-functional versus many-body Green's-function approaches, Rev. Mod. Phys. **74**, 601 (2002).

[37] L. Reining, V. Olevano, A. Rubio, and G. Onida, Excitonic effects in solids described by time-dependent density-functional theory, Phys. Rev. Lett. **88**, 066404 (2002).

[38] C. A. Ullrich, *Time-dependent density-functional theory: concepts and applications* (Oxford University Press, Oxford, 2012).

[39] A. Seidl, A. Görling, P. Vogl, J. A. Majewski, and M. Levy, Generalized Kohn-Sham schemes and the band-gap problem, Phys. Rev. B **53**, 3764 (1996).

[40] A. Görling and M. Levy, Hybrid schemes combining the Hartree-Fock method and density-functional theory: underlying formalism and properties of correlation functionals, J. Chem. Phys. **106**, 2675 (1997).

[41] R. Baer and L. Kronik, Time-dependent generalized Kohn-Sham theory, Eur. Phys. J. B **91**, 170 (2018).

[42] R. Garrick, A. Natan, T. Gould, and L. Kronik, Exact generalized Kohn-Sham theory for hybrid functionals, Phys. Rev. X **10**, 021040 (2020).

[43] A. D. Becke, Density-functional thermochemistry. III. The role of exact exchange, J. Chem. Phys. **98**, 5648 (1993).

[44] A. D. Becke, Density-functional thermochemistry. IV. A new dynamical correlation functional and implications for exact-exchange mixing, J. Chem. Phys. **104**, 1040 (1996).

[45] J. P. Perdew, M. Ernzerhof, and K. Burke, Rationale for mixing exact exchange with density functional approximations, J. Chem. Phys. **105**, 9982 (1996).

[46] P. J. Stephens, F. J. Devlin, C. F. Chabalowski, and M. J. Frisch, Ab initio calculation of vibrational absorption and circular dichroism spectra using density func-

tional force fields, J. Phys. Chem. **98**, 11623 (1994).
[47] C. Adamo and V. Barone, Toward reliable density functional methods without adjustable parameters: the PBE0 model, J. Chem. Phys. **110**, 6158 (1999).
[48] J. Heyd, G. E. Scuseria, and M. Ernzerhof, Hybrid functionals based on a screened Coulomb potential, J. Chem. Phys. **118**, 8207 (2003).
[49] A. V. Krukau, O. A. Vydrov, A. F. Izmaylov, and G. E. Scuseria, Influence of the exchange screening parameter on the performance of screened hybrid functionals, J. Chem. Phys. **125**, 224106 (2006).
[50] J. H. Skone, M. Govoni, and G. Galli, Self-consistent hybrid functional for condensed systems, Phys. Rev. B **89**, 195112 (2014).
[51] J. H. Skone, M. Govoni, and G. Galli, Nonempirical range-separated hybrid functionals for solids and molecules, Phys. Rev. B **93**, 235106 (2016).
[52] W. Chen, G. Miceli, G.-M. Rignanese, and A. Pasquarello, Nonempirical dielectric-dependent hybrid functional with range separation for semiconductors and insulators, Phys. Rev. Mater. **2**, 073803 (2018).
[53] F. Corà, M. Alfredsson, G. Mallia, D. S. Middlemiss, W. C. Mackrodt, R. Dovesi, and R. Orlando, The performance of hybrid density functionals in solid state chemistry, in *Principles and Applications of Density Functional Theory in Inorganic Chemistry II* (Springer, Berlin, 2004) pp. 171–232.
[54] J. Heyd, J. E. Peralta, G. E. Scuseria, and R. L. Martin, Energy band gaps and lattice parameters evaluated with the Heyd-Scuseria-Ernzerhof screened hybrid functional, J. Chem. Phys. **112**, 174101 (2005).
[55] I. C. Gerber, J. G. Ángyán, M. Marsman, and G. Kresse, Range separated hybrid density functional with long-range Hartree-Fock exchange applied to solids, J. Chem. Phys. **127**, 054101 (2007).
[56] T. M. Henderson, J. Paier, and G. E. Scuseria, Accurate treatment of solids with the HSE screened hybrid, Phys. Stat. Solidi B **248**, 767 (2011).
[57] M. Jain, J. R. Chelikowsky, and S. G. Louie, Reliability of hybrid functionals in predicting band gaps, Phys. Rev. Lett. **107**, 216806 (2011).
[58] M. A. L. Marques, J. Vidal, M. J. T. Oliveira, L. Reining, and S. Botti, Density-based mixing parameter for hybrid functionals, Phys. Rev. B **83**, 035119 (2011).
[59] Y.-I. Matsushita, K. Nakamura, and A. Oshiyama, Comparative study of hybrid functionals applied to structural and electronic properties of semiconductors and insulators, Phys. Rev. B **84**, 075205 (2011).
[60] J. E. Moussa, P. A. Schultz, and J. R. Chelikowsky, Analysis of the Heyd-Scuseria-Ernzerhof density functional parameter space, J. Chem. Phys. **136**, 204117 (2012).
[61] C. Friedrich, M. Betzinger, M. Schlipf, S. Blügel, and A. Schindlmayr, Hybrid functionals and GW approximation in the FLAPW method, J. Phys.: Condens. Matter **24**, 293201 (2012).
[62] M. Gerosa, C. E. Bottani, L. Caramella, G. Onida, C. Di Valentin, and G. Pacchioni, Electronic structure and phase stability of oxide semiconductors: Performance of dielectric-dependent hybrid functional DFT, benchmarked against GW band structure calculations and experiments, Phys. Rev. B **91**, 155201 (2015).
[63] Y. Hinuma, Y. Kumagai, I. Tanaka, and F. Oba, Band alignment of semiconductors and insulators using dielectric-dependent hybrid functionals: Toward high-throughput evaluation, Phys. Rev. B **95**, 075302 (2017).
[64] M.-Y. Zhang, Z.-H. Cui, Y.-C. Wang, and H. Jiang, Hybrid functionals with system-dependent parameters: Conceptual foundations and methodological developments, WIREs Comput. Mol. Sci. **10**, e1476 (2020).
[65] C. Franchini, Hybrid functionals applied to perovskites, J. Phys.: Condens. Matter **26**, 253202 (2014).
[66] Z.-H. Cui, Y.-C. Wang, M.-Y. Zhang, X. Xu, and H. Jiang, Doubly screened hybrid functional: An accurate first-principles approach for both narrow- and wide-gap semiconductors, J. Phys. Chem. Lett. **9**, 2338 (2018).
[67] T. Bischoff, J. Wiktor, W. Chen, and A. Pasquarello, Nonempirical hybrid functionals for band gaps of inorganic metal-halide perovskites, Phys. Rev. Mater. **3**, 123802 (2019).
[68] F. Zu, P. Amsalem, D. A. Egger, R. Wang, C. M. Wolff, H. Fang, M. A. Loi, D. Neher, L. Kronik, S. Duhm, and N. Koch, Constructing the electronic structure of $CH_3NH_3PbI_3$ and $CH_3NH_3PbBr_3$ perovskite thin films from single-crystal band structure measurements, J. Phys. Chem. Lett. **10**, 601 (2019).
[69] M.-H. Du, Emission Trend of Multiple Self-Trapped Excitons in Luminescent 1D Copper Halides, ACS Energy Lett. **5**, 464 (2020).
[70] J. Sun, J. Yang, and C. A. Ullrich, Low-cost alternatives to the Bethe-Salpeter equation: Towards simple hybrid functionals for excitonic effects in solids, Phys. Rev. Res. **2**, 013091 (2020).
[71] T. M. Maier, A. V. Arbuznikov, and M. Kaupp, Local hybrid functionals: Theory, implementation, and performance of an emerging new tool in quantum chemistry and beyond, WIREs Comput. Mol. Sci. **9**, e1378 (2018).
[72] R. Baer, E. Livshits, and U. Salzner, Tuned range-separated hybrids in density functional theory, Annu. Rev. Phys. Chem. **61**, 85 (2010).
[73] H. Iikura, T. Tsuneda, T. Yanai, and K. Hirao, A long-range correction scheme for generalized-gradient-approximation exchange functionals, J. Chem. Phys. **115**, 3540 (2001).
[74] B. G. Janesko, T. M. Henderson, and G. E. Scuseria, Screened hybrid density functionals for solid-state chemistry and physics, Phys. Chem. Chem. Phys. **11**, 443 (2009).
[75] J. M. Skelton, D. S. D. Gunn, S. Metz, and S. C. Parker, Accuracy of hybrid functionals with non-self-consistent Kohn–Sham orbitals for predicting the properties of semiconductors, J. Chem. Theory Comput. **16**, 3543 (2020).
[76] S. Refaely-Abramson, M. Jain, S. Sharifzadeh, J. B. Neaton, and L. Kronik, Solid-state optical absorption from optimally tuned time-dependent range-separated hybrid density functional theory, Phys. Rev. B **92**, 081204(R) (2015).
[77] J. Paier, M. Marsman, and G. Kresse, Dielectric properties and excitons for extended systems from hybrid functionals, Phys. Rev. B **78**, 121201(R) (2008).
[78] L. Bernasconi, S. Tomić, M. Ferrero, M. Rérat, R. Orlando, R. Dovesi, and N. M. Harrison, First-principles optical response of semiconductors and oxide materials, Phys. Rev. B **83**, 195325 (2011).

[79] S. Tomić, L. Bernasconi, B. G. Searle, and N. M. Harrison, Electronic and optical structure of wurtzite $CuInS_2$, J. Phys. Chem. C **118**, 14478 (2014).

[80] R. Webster, L. Bernasconi, and N. M. Harrison, Optical properties of alkali halide crystals from all-electron hybrid TD-DFT calculations, J. Chem. Phys. **142**, 214705 (2015).

[81] L. Kronik and J. B. Neaton, Excited-state properties of molecular solids from first principles, Annu. Rev. Phys. Chem. **67**, 587 (2016).

[82] D. Wing, J. B. Haber, R. Noff, B. Barker, D. A. Egger, A. Ramasubramaniam, S. G. Louie, J. B. Neaton, and L. Kronik, Comparing time-dependent density functional theory with many-body perturbation theory for semiconductors: Screened range-separated hybrids and the GW plus Bethe-Salpeter approach, Phys. Rev. Mater. **3**, 064603 (2019).

[83] A. Ramasubramaniam, D. Wing, and L. Kronik, Transferable screened range-separated hybrids for layered materials: The cases of MoS_2 and h-BN, Phys. Rev. Mater. **3**, 084007 (2019).

[84] D. K. Lewis, A. Ramasubramaniam, and S. Sharifzadeh, Tuned and screened range-separated hybrid density functional theory for describing electronic and optical properties of defective gallium nitride, Phys. Rev. Mater. **4**, 063803 (2020).

[85] Z.-H. Yang, F. Sottile, and C. A. Ullrich, A simple screened exact-exchange approach for excitonic properties in solids, Phys. Rev. B **92**, 035202 (2015).

[86] A. Tal, P. Liu, G. Kresse, and A. Pasquarello, Accurate optical spectra through time-dependent density functional theory based on screening-dependent hybrid functionals, Phys. Rev. Res. **2**, 032019 (2020).

[87] T. Sander, E. Maggio, and G. Kresse, Beyond the Tamm-Dancoff approximation for extended systems using exact diagonalization, Phys. Rev. B **92**, 045209 (2015).

[88] Y.-M. Byun and C. A. Ullrich, Excitons in solids from time-dependent density-functional theory: Assessing the Tamm-Dancoff approximation, Computation **5**, 9 (2017).

[89] Y.-M. Byun and C. A. Ullrich, Assessment of long-range-corrected exchange-correlation kernels for solids: Accurate exciton binding energies via an empirically scaled bootstrap kernel, Phys. Rev. B **95**, 205136 (2017).

[90] M. Rohlfing and S. G. Louie, Electron-hole excitations in semiconductors and insulators, Phys. Rev. Lett. **81**, 2312 (1998).

[91] L. X. Benedict, E. L. Shirley, and R. B. Bohn, Optical absorption of insulators and the electron-hole interaction: An ab initio calculation, Phys. Rev. Lett. **80**, 4514 (1998).

[92] L. X. Benedict and E. L. Shirley, Ab initio calculation of $\epsilon_2(\omega)$ including the electron-hole interaction: Application to GaN and CaF_2, Phys. Rev. B **59**, 5441 (1999).

[93] Y.-M. Byun, J. Sun, and C. A. Ullrich, Time-dependent density-functional theory for periodic solids: assessment of excitonic exchange–correlation kernels, Electron. Struct. **2**, 023002 (2020).

[94] F. Bruneval, N. Vast, and L. Reining, Effect of self-consistency on quasiparticles in solids, Phys. Rev. B **74**, 045102 (2006).

[95] J. P. Perdew, K. Burke, and M. Ernzerhof, Generalized gradient approximation made simple, Phys. Rev. Lett. **77**, 3865 (1996), erratum: *ibid.* **78**, 1396 (1997).

[96] P. Giannozzi, O. Andreussi, T. Brumme, O. Bunau, M. B. Nardelli, M. Calandra, R. Car, C. Cavazzoni, D. Ceresoli, M. Cococcioni, N. Colonna, I. Carnimeo, A. D. Corso, S. de Gironcoli, P. Delugas, R. A. D. Jr, A. Ferretti, A. Floris, G. Fratesi, G. Fugallo, R. Gebauer, U. Gerstmann, F. Giustino, T. Gorni, J. Jia, M. Kawamura, H.-Y. Ko, A. Kokalj, E. Küçükbenli, M. Lazzeri, M. Marsili, N. Marzari, F. Mauri, N. L. Nguyen, H.-V. Nguyen, A. O. de-la Roza, L. Paulatto, S. Poncé, D. Rocca, R. Sabatini, B. Santra, M. Schlipf, A. P. Seitsonen, A. Smogunov, I. Timrov, T. Thonhauser, P. Umari, N. Vast, X. Wu, and S. Baroni, Advanced capabilities for materials modelling with QUANTUM ESPRESSO, J. Phys.: Condens. Matter **29**, 465901 (2017).

[97] D. R. Hamann, Optimized norm-conserving Vanderbilt pseudopotentials, Phys. Rev. B **88**, 085117 (2013), erratum: *ibid.* **95**, 239906 (2017).

[98] M. van Setten, M. Giantomassi, E. Bousquet, M. Verstraete, D. Hamann, X. Gonze, and G.-M. Rignanese, The pseudodojo: Training and grading a 85 element optimized norm-conserving pseudopotential table, Comput. Phys. Commun. **226**, 39 (2018).

[99] N. Troullier and J. L. Martins, Efficient pseudopotentials for plane-wave calculations, Phys. Rev. B **43**, 1993 (1991).

[100] See Supplemental Material at http://... for the following details: (1) Discussion of the choice of pseudopotentials. (2) Comparison of LDA and PBE band structures. (3) Comparison of G_0W_0@LDA and G_0W_0@PBE band structures. (4) Discussion of single-shot DDH1 and DDH2 band gaps. (5) Convergence tests.

[101] D. Sangalli, A. Ferretti, H. Miranda, C. Attaccalite, I. Marri, E. Cannuccia, P. Melo, M. Marsili, F. Paleari, A. Marrazzo, G. Prandini, P. Bonfà, M. O. Atambo, F. Affinito, M. Palummo, A. Molina-Sánchez, C. Hogan, M. Grüning, D. Varsano, and A. Marini, Many-body perturbation theory calculations using the yambo code, J. Phys.: Condens. Matter **31**, 325902 (2019).

[102] M. S. Hybertsen and S. G. Louie, Electron correlation in semiconductors and insulators: Band gaps and quasiparticle energies, Phys. Rev. B **34**, 5390 (1986).

[103] R. W. Godby and R. J. Needs, Metal-insulator transition in Kohn-Sham theory and quasiparticle theory, Phys. Rev. Lett. **62**, 1169 (1989).

[104] A. Marini and R. Del Sole, Dynamical excitonic effects in metals and semiconductors, Phys. Rev. Lett. **91**, 176402 (2003).

[105] P. Larson, M. Dvorak, and Z. Wu, Role of the plasmon-pole model in the GW approximation, Phys. Rev. B **88**, 125205 (2013).

[106] D. Kammerlander, S. Botti, M. A. L. Marques, A. Marini, and C. Attaccalite, Speeding up the solution of the Bethe-Salpeter equation by a double-grid method and Wannier interpolation, Phys. Rev. B **86**, 125203 (2012).

[107] M. R. Filip and F. Giustino, *GW* quasiparticle band gap of the hybrid organic-inorganic perovskite $CH_3NH_3PbI_3$: Effect of spin-orbit interaction, semicore electrons, and self-consistency, Phys. Rev. B **90**, 245145 (2014).

[108] L. Leppert, T. Rangel, and J. B. Neaton, Towards predictive band gaps for halide perovskites: Lessons from

one-shot and eigenvalue self-consistent GW, Phys. Rev. Mater. **3**, 103803 (2019).

[109] P. Romaniello, D. Sangalli, J. A. Berger, F. Sottile, L. G. Molinari, L. Reining, and G. Onida, Double excitations in finite systems, J. Chem. Phys. **130**, 044108 (2009).

[110] X. Blase, I. Duchemin, and D. Jacquemin, The Bethe-Salpeter equation in chemistry: relations with TD-DFT, applications and challenges, Chem. Soc. Rev. **47**, 1022 (2018).